Journal of Computational and Applied Mathematics 336 (2018) 425–438

Contents lists available at ScienceDirect

Journal of Computational and Applied Mathematics

journal homepage: www.elsevier.com/locate/cam

Regularized iterative Weiner filter method for blind image deconvolution☆

Fang Li [a], Xiao-Guang Lv [b,*], Ziwei Deng [a]

[a] Department of Mathematics, East China Normal University, Shanghai, China
[b] School of Science, Huaihai Institute of Technology, Lianyungang, Jiangsu, China

ARTICLE INFO

Article history:
Received 24 May 2017
Received in revised form 4 September 2017

Keywords:
Weiner filter
Blind image deconvolution
Regularization
Iterative algorithm
Microscopic image

ABSTRACT

Blind image deconvolution is a highly ill-posed problem. As a generalization of the well known Weiner filter, the existing iterative Weiner filter (IWF) method for blind image deconvolution is unstable and suffers from serious ringing artifacts. To overcome these drawbacks, in this paper, we propose two novel regularized iterative Weiner filter methods. We assume that both the latent image and the convolution kernel can be estimated by applying two different filters on the observed image. To estimate the filters, we propose to minimize energy functionals combined by the mean square errors with some regularization terms. Both H^1 and total variation (TV) regularization are considered. By applying alternating minimization method and operator splitting technique, we derive iterative algorithms for each regularization method. The proposed methods are effective for blind deconvolution of Gaussian blurred images which is widely observed in real applications such as microscopic images. Numerical experimental results on both synthetic images and real microscopic images are presented. The comparisons show that the proposed regularized algorithms perform better than the closely related state-of-the-art methods in terms of peak signal-to-noise ratio (PSNR) and visual quality.

1. Introduction

Blind image deconvolution is the problem of recovering a sharp version of an input blurry image when the blur kernel is unknown [1]. Blind deconvolution is performed for image restoration in many applications such as astronomical speckle imaging, remote sensing, and medical imaging [2]. Mathematically, the blind image deconvolution problem can be formulated as

$$y = h \star x + \eta \tag{1}$$

where $\star$ represents the two-dimensional convolution operation, y is the observed blurred image, η is the additive white Gaussian noise, x is the latent sharp image and h is the blur kernel whose support is small compared to the image size. The problem is highly ill-posed since there are infinite pairs of solutions. To get the ideal solution, some additional assumptions on x and h must be introduced.

In recent years, a wide range of blind deconvolution methods have been developed as generalization of nonblind deconvolution methods. The earliest classic methods for nonblind image deconvolution include the Weiner filter [3,4]

☆ This work is supported by the National Science Foundation of China (11671002, 61731009), the Science and Technology Commission of Shanghai Municipality (STCSM) (13dz2260400), NSF of HHIT (Z2017004), Jiangsu Key Lab for NSLSCS (201806), Qing Lan Project and Hai Yan Project.

* Corresponding author.
E-mail addresses: fli@math.ecnu.edu.cn (F. Li), xiaoguanglv@hhit.edu.cn (X.-G. Lv).

https://doi.org/10.1016/j.cam.2017.12.026
0377-0427/

and the Richardson–Lucy algorithm [5,6]. The Weiner filter works in the frequency domain, attempting to minimize the impact of deconvolved noise at frequencies. The Wiener filter nonblind deconvolution method has widespread use in image deconvolution applications, as the frequency spectrum of most visual images is fairly well behaved and may be estimated easily. Later, Ayers and Dainty generalized the Weiner filter to blind image deconvolution by estimating both the latent image and the blur kernel in a similar way as the Weiner filter, which is essentially an iterative Weiner filter (IWF) algorithm [7]. The IWF algorithm is simple and effective for some special images. However, the disadvantage of IWF is that it is not stable and has serious ringing artifacts in many applications. To overcome these drawbacks, Tofighi et al. proposed a new blind deconvolution algorithm for microscopic images based on IWF by adding two convex sets constraints [8]. One is phase constraint in the Fourier domain and the other is epigraph set of total variation (ESTV) constraint in the spatial domain. The constraints are implemented by projection on convex sets. This algorithm is named as IWF-Phase&ESTV in this paper. IWF-Phase&ESTV is more stable than IWF. However, the restoration quality is still limited. In addition, IWF with only phase constraint or ESTV constraint are also studied in [8], which are named as IWF-Phase and IWF-ESTV respectively. Similar to the Weiner filter algorithm, Richardson–Lucy algorithm is generalized to blind deconvolution [9,10] and regularization versions are also studied [11–13].

Another category of methods for blind deconvolution are based on variational models. These models commonly include a regularization term and a data fitting term. In the regularization term, one requires that the image should follow some prior distribution. The widely used image priors are sparsity of image under some transform such as gradient transform, wavelet transform, tight frame transform or patch based transform. Gradient sparsity prior is studied in many works with different norms. In [14], H^1 regularization is considered for both the latent image x and the blur kernel h. In [15], total variation (TV) regularization [16] is used for x and h. A normalized sparsity measure with ℓ^1/ℓ^2 norm is considered in [17]. Nonconvex ℓ^p, $0 < p < 1$ norm is used for gradient of x in [18]. Unnatural ℓ^0 norm for gradient of x is considered in [19]. ℓ^0 norm of both gradient and intensity prior for x is proposed in [20] for text blind image deconvolution. Sparsity of framelet coefficients regularization are adopted in [21,22]. Patch based low-rank prior is considered for both the image x and its gradient [23]. ℓ^2 norm prior is commonly used for blur kernel h in the above references. Additionally, mean square error term is commonly used for data fitting. Numerically, gradient descent method can be used [14,15,24]. To speed up, fast alternating minimization algorithms are designed for blind deconvolution based on the split Bregman (SB) method or alternating direction method of multipliers (ADMM) [25,22,26,20]. The other optimization techniques [27–30] can also be incorporated to solve these problems in real application. Remarkable results are reported for some of the above variational methods especially for sparse blur kernel. However, they are unlikely to work well for Gaussian blurred images such as the microscopic images in which the kernel is dense.

In order to increase stability and suppress ringing artifacts in the IWF type method, in this paper, we propose two novel regularized iterative Weiner filter methods for blind deconvolution of microscopic images. We reformulate the IWF based blind deconvolution method into a variational model such that it is flexible for us to add regularization terms. We consider both H^1 and TV regularization terms incorporating the nonnegative and normalization constraints of blur kernel. By using alternating minimization and ADMM algorithm, we derive efficient algorithms for both models. Experiments show that the proposed algorithms are superior to the closely related methods in terms of restoration quality and stability.

The paper is organized as follows. In Section 2, we review the IWF algorithm and its extensions. In Section 3, we propose our blind deconvolution variational models with H^1 and TV regularization based on IWF. Then we derive the iterative algorithms of the proposed models. We present our experimental results in Section 4 and give the conclusion in Section 5.

2. IWF algorithm and its extensions

Denote $n = (n_1, n_2)$ as the coordinate in spatial domain and $\omega = (\omega_1, \omega_2)$ as the coordinate in frequency domain. Then the spatial image degradation model (1) can be rewritten as

$$y(n) = h(n) \star x(n) + \eta(n). \tag{2}$$

We know from the convolution theorem that the Fourier transform of the product of two functions in the spatial domain is the convolution of the transforms of the two functions in the frequency domain. Thus by applying the Fourier transform on Eq. (2), we get the image degradation model in the frequency domain

$$Y(\omega) = H(\omega)X(\omega) + N(\omega) \tag{3}$$

where Y, H, X and N denote the Fourier transforms of y, h, x and η, respectively. The IWF algorithm [7] for blind deconvolution updates the latent image x and the blur kernel h iteratively in a Weiner filter-like equation, which is given in the following Algorithm 1.

Note that in Algorithm 1, $\mathcal{F}$ denotes the Fourier transform, $\mathcal{F}^{-1}$ denotes the inverse Fourier transform, α is a small real number, and * denotes the conjugate operator. In Algorithm 1, two projections on convex sets $\mathcal{C}_1$ and $\mathcal{C}_2$ are required to impose the image constraint and kernel constraint respectively, which are defined as

$$\mathcal{C}_1 := \{x | 0 \le x(n) \le 1, \forall\, n\} \tag{4}$$

Algorithm 1 IWF algorithm for blind deconvolution

- Initialization: $X^0 = \mathcal{F}(x^0)$, $H^0 = \mathcal{F}(h^0)$.
- For $k = 0, 1, \ldots$, repeat until stopping criterion is reached

$$X^{k+1} = \mathcal{F}\mathcal{P}_1\mathcal{F}^{-1}\left(\frac{H^{k*}Y}{|H^k|^2+\alpha/|X^k|^2}\right),$$
$$H^{k+1} = \mathcal{F}\mathcal{P}_2\mathcal{F}^{-1}\left(\frac{X^{k*}Y}{|X^k|^2+\alpha/|H^k|^2}\right).$$

- Output: $x^{k+1} = \mathcal{F}^{-1}(X^{k+1})$, $h^{k+1} = \mathcal{F}^{-1}(H^{k+1})$.

and

$$\mathcal{C}_2 := \{h | h \geq 0, \sum_n h(n) = 1\}. \tag{5}$$

The projection operators on sets $\mathcal{C}_1$ and $\mathcal{C}_2$ are simplified as

$$\mathcal{P}_1 = \mathrm{Proj}_{\mathcal{C}_1}, \mathcal{P}_2 = \mathrm{Proj}_{\mathcal{C}_2}.$$

Based on the observation that most blurring functions in microscopy images are symmetric with respect to the origin and such that the phase of Fourier transform is not modified, the IWF-Phase algorithm [8] improves the IWF algorithm by adding a phase constraint. Meanwhile, TV constraint in the spatial domain for both the latent image and the blur kernel can also be incorporated, which is called IWF-ESTV [8]. If both constraints are used, the algorithm is called IWF-Phase&ESTV [8]. Both constraints are implemented directly by projection on convex sets. The details are omitted here.

3. The proposed methods

In this section, we propose the regularized iterative Weiner filter methods with H^1 and TV regularization respectively, which are called IWF-H^1 and IWF-TV for short.

Let us give the basic assumption of our methods. In the image degradation model (1), h and x play a similar role since the convolution can be changed in the continuous setting, that is, $h \star x = x \star h$. Inspired by the basic idea of the Weiner filter for the nonblind deconvolution problem, we assume that both the latent sharp image and the blur kernel can be obtained by convolution the observed image with unknown filters g_1 and g_2, respectively. In other words, we assume that the latent image and the blur kernel can be estimated by

$$x = g_1 \star y, \ h = g_2 \star y. \tag{6}$$

such that x and h satisfy the constraints $x \in \mathcal{C}_1$ and $h \in \mathcal{C}_2$, where g_1 and g_2 are filters. Our aim is to get the filters g_1 and g_2, and then recover x and h. In the following subsections, we give the details of our regularization methods for blind image deconvolution.

3.1. IWF-H^1

To estimate the filters g_1 and g_2, we propose to minimize the square errors of the assumption (6) and incorporate H^1 regularization terms, which gives the following energy minimization model

$$\min_{g_1,g_2} \left\{ \begin{array}{l} \|x - g_1 \star y\|_2^2 + \epsilon\|g_1 \star x\|_2^2 + \lambda\|\nabla(g_1 \star x)\|_2^2 + \\ \|h - g_2 \star y\|_2^2 + \epsilon\|g_2 \star h\|_2^2 + \lambda\|\nabla(g_2 \star h)\|_2^2 \end{array} \right\} \tag{7}$$

where $\nabla = (\nabla_h, \nabla_v)$ is the gradient operator combined by difference operators along horizontal and vertical directions. The last two terms in each row are regularization terms which ask that $g_1 \star x$ and $g_2 \star h$ should be smooth in H^1 sense. Note that our regularization terms are different from those widely used in existing literatures for blind deconvolution. The existing regularization usually performs on the latent image x and the blur kernel h directly. While in model (7) we regularize the filtered version of x and h such that these terms can contribute to the estimation of g_1 and g_2.

In the Fourier domain, model (7) is equivalent to

$$\min_{G_1,G_2} \left\{ \begin{array}{l} \|X - G_1Y\|_2^2 + \epsilon\|G_1X\|_2^2 + \lambda\|DG_1X\|_2^2 + \\ \|H - G_2Y\|_2^2 + \epsilon\|G_2H\|_2^2 + \lambda\|DG_2H\|_2^2 \end{array} \right\} \tag{8}$$

where $G_1, G_2, D = (D_h, D_v)$ denote the Fourier transforms of g_1, g_2 and $\nabla = (\nabla_h, \nabla_v)$ respectively, and

$$\|DG_1X\|_2^2 = \|D_hG_1X\|_2^2 + \|D_vG_1X\|_2^2.$$

Firstly, we derive the optimal condition for G_1 in the following. Assume that the latent image x and the noise η are independent, i.e., $\langle X, N\rangle = 0$. By using Eq. (3), we have the equality

$$\|X - G_1Y\|_2^2 = \|(1 - G_1H)X\|_2^2 + \|G_1N\|_2^2$$

Then the subproblem of G_1 is equivalent to

$$\min_{G_1} \left\{ \|(1 - G_1H)X\|_2^2 + \|G_1N\|_2^2 + \epsilon\|G_1X\|_2^2 + \lambda\|DG_1X\|_2^2 \right\}. \tag{9}$$

By taking the Wirtinger derivative of functional in (9) with respect to G_1 and setting the result to be zero, we get the optimal condition of G_1 as follows

$$-H(1 - G_1^*H^*)|X|^2 + G_1^*|N|^2 + \epsilon G_1^*|X|^2 + \lambda G_1^*|D|^2|X|^2 = 0$$

where $|D|^2 = |D_h|^2 + |D_v|^2$. For simplicity, we set the spectral of $|N|^2$ to be a constant α since the noise is white Gaussian noise in (1). Then the above equality gives the solution of G_1^*

$$G_1^* = \frac{H}{|H|^2 + \alpha/|X|^2 + \epsilon + \lambda|D|^2}.$$

Equivalently, we have

$$G_1 = \frac{H^*}{|H|^2 + \alpha/|X|^2 + \epsilon + \lambda|D|^2}. \tag{10}$$

By a similar argument, we can derive the solution of G_2

$$G_2 = \frac{X^*}{|X|^2 + \alpha/|H|^2 + \epsilon + \lambda|D|^2}. \tag{11}$$

Then, X and H can be estimated alternatingly by applying filter G_1 and G_2 on the given data Y respectively, i.e.,

$$X = G_1Y = \frac{H^*Y}{|H|^2 + \alpha/|X|^2 + \epsilon + \lambda|D|^2}, \tag{12}$$

$$H = G_2Y = \frac{X^*Y}{|X|^2 + \alpha/|H|^2 + \epsilon + \lambda|D|^2}. \tag{13}$$

Finally, by incorporating the convex constraints of the latent image and the blur kernel as in the IWF algorithm, we get the following H^1 regularized version in Algorithm 2, which is called the IWF-H^1 algorithm.

Algorithm 2 IWF-H^1 algorithm for blind deconvolution

- Initialization: $X^0 = \mathcal{F}(x^0)$, $H^0 = \mathcal{F}(h^0)$.
- For $k = 0, 1, \ldots$, repeat until stopping criterion is reached

$$X^{k+1} = \mathcal{F}\mathcal{P}_1\mathcal{F}^{-1}\left(\frac{H^{k*}Y}{|H^k|^2+\alpha/|X^k|^2 + \epsilon + \lambda|D|^2}\right),$$

$$H^{k+1} = \mathcal{F}\mathcal{P}_2\mathcal{F}^{-1}\left(\frac{X^{k+1*}Y}{|X^{k+1}|^2+\alpha/|H^k|^2 + \epsilon + \lambda|D|^2}\right).$$

- Output: $x^{k+1} = \mathcal{F}^{-1}(X^{k+1})$, $h^{k+1} = \mathcal{F}^{-1}(H^{k+1})$.

Note that in the IWF-H^1 algorithm, the updated X^{k+1} is used in the updating of H^{k+1}. While in the IWF algorithm, X^k is used in the updating of H^{k+1}. As observed in our experiments, using X^{k+1} in the updating of H^{k+1} increases stability of the algorithm.

3.2. IWF-TV

TV regularization was firstly introduced for image denoising in the seminal work [16], and since then it has been applied successfully in many image processing applications including nonblind or blind image deconvolution [31,15,11,25,24,8,32,33]. In this subsection, we consider to use the TV regularization instead of the H^1 regularization in our framework. That is, we propose the following energy minimization model

$$\min_{g_1,g_2} \left\{ \begin{matrix} \|x - g_1 \star y\|_2^2 + \epsilon\|g_1 \star x\|_2^2 + \lambda\|\nabla(g_1 \star x)\|_1 + \\ \|h - g_2 \star y\|_2^2 + \epsilon\|g_2 \star h\|_2^2 + \lambda\|\nabla(g_2 \star h)\|_1 \end{matrix} \right\} \tag{14}$$

where $\|\nabla(g_1 \star x)\|_1$ and $\|\nabla(g_2 \star h)\|_1$ are TV regularization terms.

For this model, we have no closed-form solutions for g_1 and g_2. Hence we use the operator splitting technique to split the original problem into easier subproblems. We remark that the ADMM algorithm and the primal–dual type algorithm [34,35] are very popular and can be used to derive efficient algorithms for our problem. Since the performances of both algorithms are similar, we choose ADMM in this paper. Note that the problems for g_1 and g_2 are separable. We here only consider the subproblem of g_1

$$\min_{g_1} \left\{ \|x - g_1 \star y\|_2^2 + \epsilon \|g_1 \star x\|_2^2 + \lambda \|\nabla(g_1 \star x)\|_1 \right\}. \tag{15}$$

Firstly, by adding extra variable u_1, we rewrite (15) as a constrained problem

$$\begin{aligned} &\min_{g_1} \left\{ \|x - g_1 \star y\|_2^2 + \epsilon \|g_1 \star x\|_2^2 + \lambda \|u\|_1 \right\} \\ &\text{s.t.} \quad \nabla g_1 \star x = u_1. \end{aligned}$$

Using the ADMM method, we get the following iteration scheme

$$(g_1, u_1) \leftarrow \arg\min_{g_1, u_1} \mathcal{L}(g_1, u_1, v_1) \tag{16}$$

$$v_1 \leftarrow v_1 + \nabla g_1 \star x - u_1 \tag{17}$$

where

$$\mathcal{L} = \|x - g_1 \star y\|_2^2 + \epsilon \|g_1 \star x\|_2^2 + \lambda \|u\|_1 + \mu \|\nabla g_1 \star x - u_1 + v_1\|_2^2$$

and μ is a constant parameter. The problem (16) is then solved by the following alternating minimization method.

3.2.1. Solving g_1-subproblem

For fixed u_1, the subproblem for g_1 can be rewritten as

$$\min_{G_1} \|X - G_1 Y\|_2^2 + \epsilon \|G_1 X\|_2^2 + \mu \|D G_1 X - U_1 + V_1\|_2^2 \tag{18}$$

in the Fourier domain, where U_1 and V_1 are Fourier transforms of u_1 and v_1. By taking the Wirtinger derivative of the functional in (18) with respect to G_1 and setting the result to be zero, we get the closed-form solution

$$G_1^* = \frac{H + \frac{\mu D X (U^* - V^*)}{|X|^2}}{|H|^2 + \frac{\sigma^2}{|X|^2} + \epsilon + \mu |D|^2}.$$

3.2.2. Solving u_1-subproblem

For fixed g_1, the subproblem for u_1 is

$$\min_{u_1} \lambda \|u_1\|_1 + \mu \|\nabla g_1 \star x - u_1 + v_1\|_2^2.$$

It is well known that the closed-form solution of this subproblem can be expressed using the soft shrinkage [36,37], that is,

$$u_1 = \text{shrink}(\nabla g_1 \star x + v_1, \tau)$$

where $\tau = \frac{\lambda}{2\mu}$ and shrink is the soft shrinkage operator defined as

$$\text{shrink}(v, \tau) := \max(|v| - \tau, 0)\, \text{sign}(v).$$

Similar as the above calculation, by using two extra variables u_2 and v_2, which play the similar role as u_1 and v_1, we can get the closed-form solutions of g_2 and u_2 respectively.

Finally, by incorporating the convex constraints of the latent image and the blur kernel, we get the proposed IWF-TV algorithm for blind image deconvolution in Algorithm 3. Note that in Algorithm 3, the capital letters and corresponding small letters denote the Fourier transform pairs. For instance, X^{k+1} and x^{k+1} is a Fourier transform pair.

We remark that other regularization techniques such as tight frame wavelets [38], nonlocal TV [39], high order TV [40,41] can also be used in the proposed variational models. The algorithms will be different for each regularization. We leave it as our future work.

4. Experimental results

In this section, we give the experimental results of the proposed algorithms and compare them with the other six methods. Four of them are IWF type methods including IWF in [7], IWF-Phase, IWF-ESTV, IWF-Phase&ESTV in [8], which are the most closely related algorithms with ours. The other two methods are the state-of-the-art blind image deconvolution methods including the normalized sparsity measure based method in [17] and the ℓ^0 norm based method in [20].

Algorithm 3 IWF-TV algorithm for blind deconvolution

- Initialization: x^0, h^0.
- For $k = 0, 1, \ldots$, repeat until stopping criterion is reached

$$
\begin{aligned}
G_1^{k+1} &= \frac{H^{k*} + \mu D^* X^{k*}(U_1^k - V_1^k)/|X^k|^2}{|H^k|^2 + \alpha/|X^k|^2 + \epsilon + \mu|D|^2},\\
x^{k+1} &= \mathcal{P}_1\mathcal{F}^{-1}(G_1^{k+1}Y),\\
u_1^{k+1} &= \text{shrink}(\nabla g_1^{k+1} \star x^{k+1} + v_1^k, \tau),\\
v_1^{k+1} &= v_1^k + \nabla g_1^{k+1} \star x^{k+1} - u_1^{k+1},\\
G_2^{k+1} &= \frac{X^{k+1*} + \mu D^* H^{k*}(U_2^k - V_2^k)/|H^k|^2}{|X^{k+1}|^2 + \alpha/|H^k|^2 + \epsilon + \mu|D|^2},\\
h^{k+1} &= \mathcal{P}_2\mathcal{F}^{-1}(G_2^{k+1}Y),\\
u_2^{k+1} &= \text{shrink}(\nabla g_2^{k+1} \star h^{k+1} + v_2^k, \tau),\\
v_2^{k+1} &= v_2^k + \nabla g_2^{k+1} \star h^{k+1} - u_2^{k+1}.
\end{aligned}
$$

- Output: x^{k+1}, h^{k+1}.

The peak signal-to-noise ratio (PSNR) is adopted to measure the quality of the blind deconvolution results, which is defined as

$$\text{PSNR}(x, x_{true}) = 10 \log 10 \left(\frac{255^2}{\frac{1}{st}\|x - x_{true}\|_2^2} \right)$$

where x is the restored image and x_{true} is the true image, s and t are numbers of row and column of the image. Note that PSNR is a standard image quality measure which is widely used in comparing image restoration results.

We initialize $h^0 = \delta$ and $x^0 = y$ in our algorithms, where δ is the Dirac function. Our algorithms are not sensitive to the initial guess of the image and the kernel. The stopping criterion for our algorithms is that the maximum iteration is reached or the relative error between the successive iterate of the restored image satisfies the following inequality

$$\frac{\|x^{k+1} - x^k\|_2}{\|x^{k+1}\|_2} < 10^{-4}.$$

The maximum iteration is set as 300 for the gray scale image, and 50 for the color image. The other parameters are set as follows. IWF-H[1]: $\alpha = 10^{-3}$, $\lambda = 10^{-5}$, $\epsilon = 0$ for the gray image and $\epsilon = 10^{-5}$ for the color image; IWF-TV: $\alpha = 10^{-3}$, $\epsilon = 10^{-5}$, $\lambda = 10^{-7}$, $\mu = 0.5 \times 10^{-6}$. The parameters of the proposed algorithms are chosen by trial and error. The rationales on the choice of parameters are as follows. In our algorithms, α denotes the spectral of $|N|^2$ which can be estimated from the noise level. μ is the penalty parameter in ADMM for equality constraints which can be chosen according to the general ADMM algorithm. λ and ϵ are regularization parameters which are very important in our algorithms. Bigger λ and ϵ lead to smoother deblurred images and more stability of the algorithms. However, too big λ and ϵ will oversmooth the image details and decrease the restoration quality. For methods IWF, IWF-Phase, IWF-ESTV and IWF-Phase&ESTV, we use the MATLAB source code from the authors in [8].[1] For methods in [17] and [20], we use the MATLAB source codes from the authors.[2,3] For fair comparison, the parameters are tuned to get optimal results for each method. To reduce ringing artifacts, we add black boundaries with 50 pixel in each side of the test images in all experiments.

All the experiments are performed under Windows 8 and MATLAB R2012a with Intel Core i7-4500 CPU@1.80 GHz and 8 GB memory. The programming language is MATLAB for all methods for fair comparison.

4.1. Tests on simulated images

We use two simulated data sets in our experiments which are widely used in literatures. The first data set is shown in Fig. 1. Fig. 1(a) is the standard test image Lena. Fig. 1(b) is the blurry version of Fig. 1(a). The blur kernel is Gaussian kernel generated by Matlab routine fspecial('gaussian', 30, 5). That is, the kernel follows Gaussian distribution with standard deviation 5 and the kernel size is 30×30.

1 http://signal.ee.bilkent.edu.tr/BlindDeconvolution.html.

2 http://cs.nyu.edu/~dilip/research/blind-deconvolution/.

3 https://sites.google.com/site/jspanhomepage/l0rigdeblur.

(a) (b) PSNR = 22.66 dB.

Fig. 1. The first simulated test data set. (a) Lena image; (b) the blurred image degraded by Gaussian blur with standard deviation 5 and size 30×30.

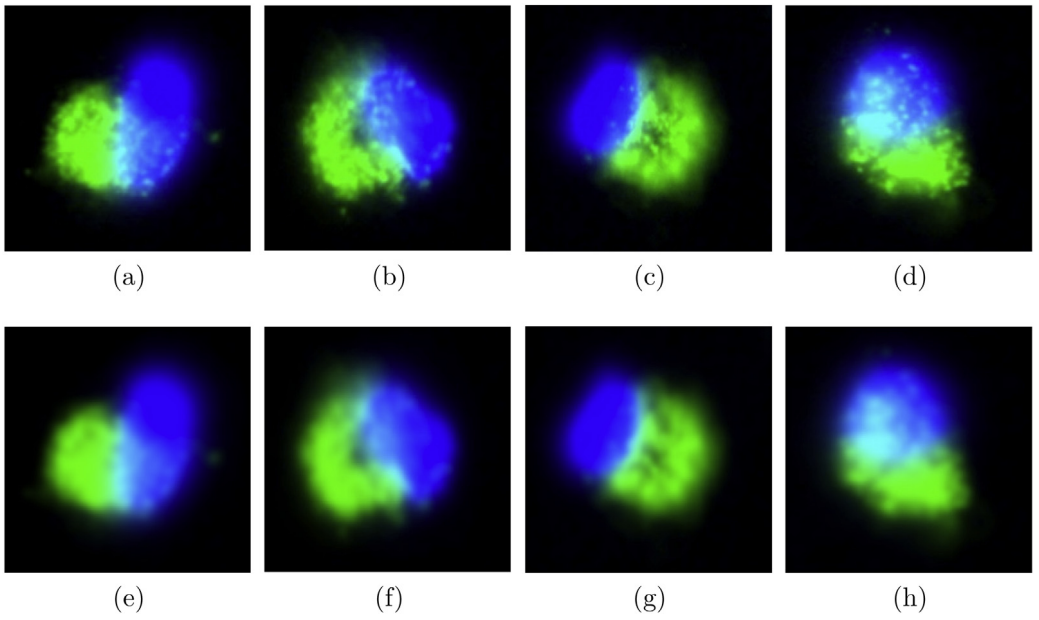

Fig. 2. The second simulated test data set. (a)–(d) are some of the sample fluorescent labeled mouse liver tissue microscopic images: (a) Im-5; (b) Im-6; (c) Im-7; (d) Im-8; (e)–(h) are the blurred images of (a)–(d) degraded by Gaussian blur with standard deviation 3 and size 20×20.

The test images in the second data set are microscopic images. Note that following [8,42,43], we use rotationally symmetric Gaussian kernel to simulate the blur kernel in microscopic images. Fig. 2 shows some of the fluorescent labeled mouse liver tissue microscopic images in the second test data set, which are also used in [8] and [44]. Fig. 2(a)–(d) are the microscopic images and Fig. 2(e)–(h) are the corresponding simulated blurred images, in which the blur kernel is generated by fspecial('gaussian', 20, 3).

In Fig. 3, we display the blind deconvolution results of eight methods applied on the blurred Lena image in Fig. 1(b). The PSNR values and computational time are reported below the images or in the caption. For IWF, IWF-Phase, IWF-ESTV, and IWF-Phase&ESTV, the algorithms stop when the iterations attain the maximum 300. Actually, the relative error is relatively large for these four methods and cannot reach the tolerance. For the proposed IWF-H^1 and IWF-TV, the algorithms stop when the relative error attains the tolerance. The iterations are 245 and 112 respectively. By carefully observing the deconvolution results, we find that the results of IWF, IWF-Phase and IWF-ESTV, as shown in Fig. 3(a)–(c), have serious ringing artifacts. The result of IWF-Phase&ESTV in Fig. 3(d) is better than the first three, in which the ringing artifacts are alleviated. The results of methods in [17] and [20] are oversmoothed, see the edges and the details of the hair in Fig. 4(e)–(f). The results of the proposed algorithms are displayed in Fig. 3(g)–(h), in which the edges and details are well recovered and the ringing artifacts are well suppressed. In terms of image quality measure, the proposed IWF-H^1 has the highest PSNR value among all, and IWF-TV is the second best.

In Fig. 4, we display the PSNR vs. Iterations curves for six IWF type methods corresponding to some of the results in Fig. 3. The PSNR curves of IWF, IWF-Phase, IWF-ESTV, and IWF-Phase&ESTV are seriously oscillating which implies that these four

(a) PSNR = 25.09 dB. (b) PSNR = 21.81 dB. (c) PSNR = 24.99 dB.

(d) PSNR = 25.37 dB. (e) PSNR = 25.57 dB. (f) PSNR = 25.04 dB.

(g) PSNR = 26.40 dB. (h) PSNR = 25.81 dB.

Fig. 3. Test on the blurred Lena image Fig. 1(b). (a) The result of IWF, iterations = 300, computational time = 170 s; (b) the result of IWF-Phase, iterations = 300, computational time = 228 s; (c) the result of IWF-ESTV, iterations = 300, computational time = 335 s; (d) the result of IWF-Phase&ESTV, iterations = 300, computational time = 375 s; (e) the result of method in [17], computational time = 97 s; (f) the result of method in [20], computational time = 161 s; (g) the result of the proposed IWF-H^1, iterations = 245, computational time = 146 s; (h) the result of the proposed IWF-TV, iterations = 112, computational time = 172 s.

algorithms are not stable, see Fig. 4(a)–(d). Accordingly, the curves of relative error vs. iterations are also oscillating. By contrast, the PSNR curves of the proposed algorithms IWF-H^1 and IWF-TV in Fig. 4(e)–(f) are smooth and monotonically increasing, which implies the stability and the convergence of the proposed algorithms.

In the second test, we use 14 blurred microscopic images. Some of the images are displayed in Fig. 2. We report the PSNR values of eight methods in Table 1 and display the deblurred images of im-7 in Fig. 5 as an example. In Table 1, the highest PSNR values are marked in bold. The best PSNR are achieved by the proposed IWF-H^1 or IWF-TV for each image. Averagely, the PSNR values of IWF-H^1 and IWF-TV are very close, which are at least 2 dB higher than the other methods. Among the four methods including IWF, IWF-Phase, IWF-ESTV and IWF-Phase&ESTV, IWF-Phase&ESTV performs the best while IWF is the poorest. The methods in [17] and [20] have much lower PSNR values than others, which implies that they are not suitable for deconvolution of Gaussian blurred images.

For visual comparison, in Fig. 5, we display the deconvolution results of IWF, IWF-Phase&ESTV, the methods in [17] and [20], and the proposed algorithms. As shown in Fig. 5(a), the ringing artifacts are serious in the result of IWF. In the

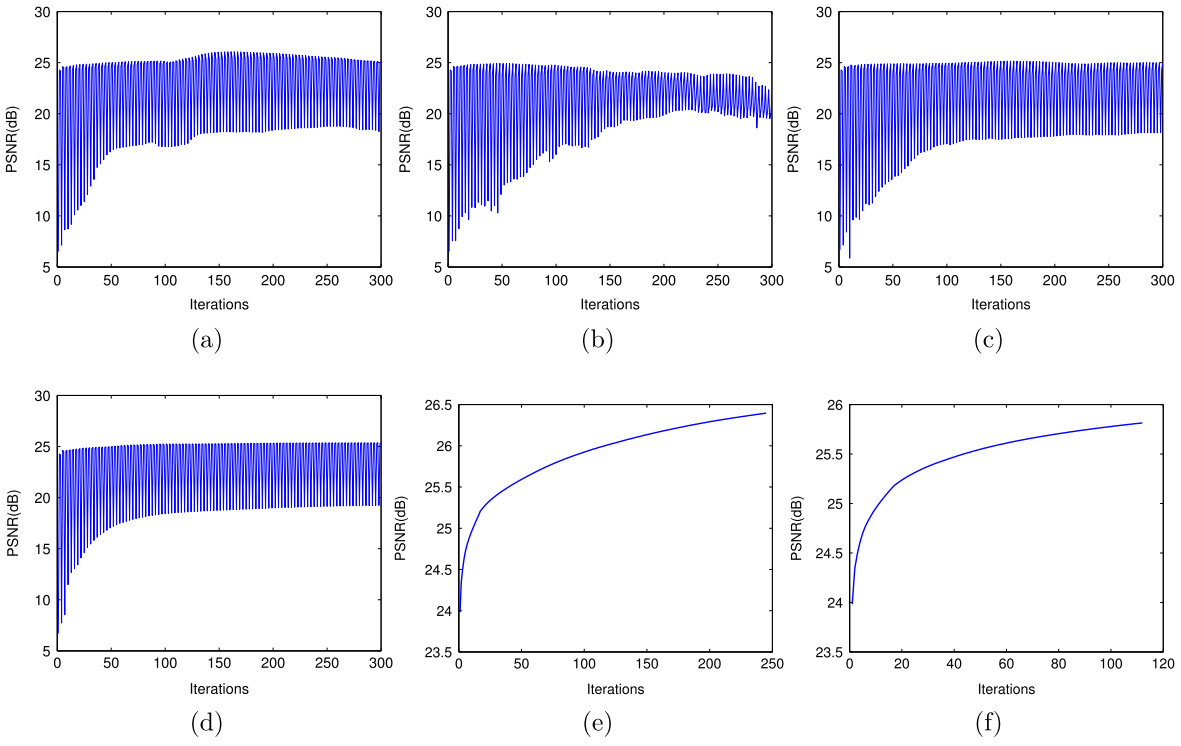

Fig. 4. The comparison of PSNR vs. Iterations curves of different methods. (a) IWF; (b) IWF-Phase; (c) IWF-ESTV; (d) IWF-Phase&ESTV, (e) IWF-H^1, (f) IWF-TV.

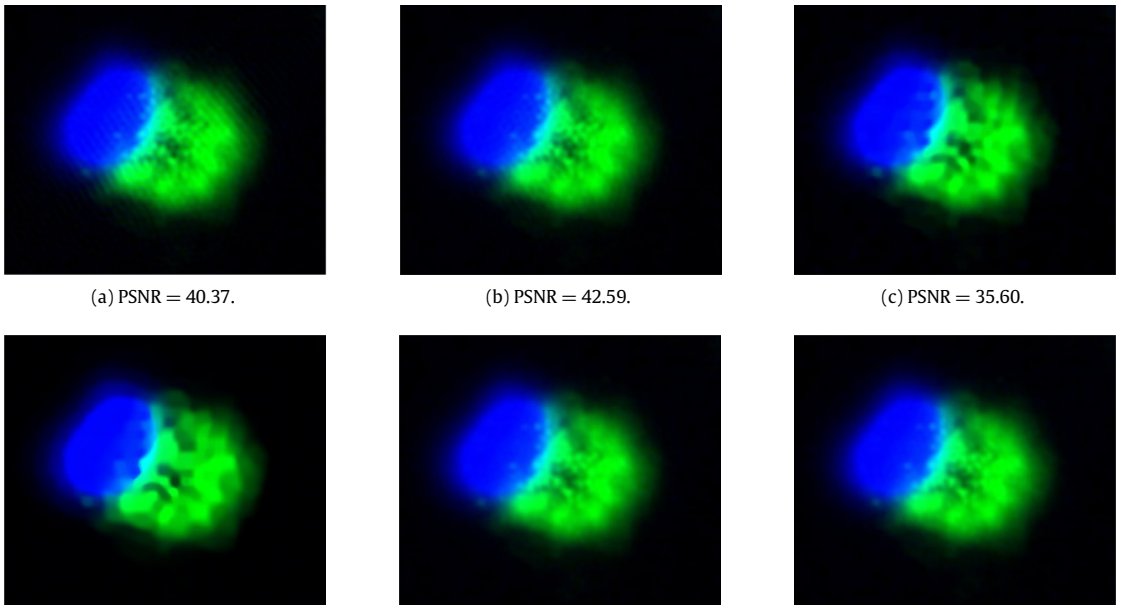

(a) PSNR = 40.37. (b) PSNR = 42.59. (c) PSNR = 35.60.

(d) PSNR = 33.62. (e) PSNR = 44.79. (f) PSNR = 44.70.

Fig. 5. Test on simulated blurry microscopic images in Fig. 2(g). (a) The result of IWF; (b) the result of IWF-Phase&ESTV; (c) the result of method in [17]; (f) the result of method in [20]; (g) the result of the proposed IWF-H^1; (h) the result of the proposed IWF-TV.

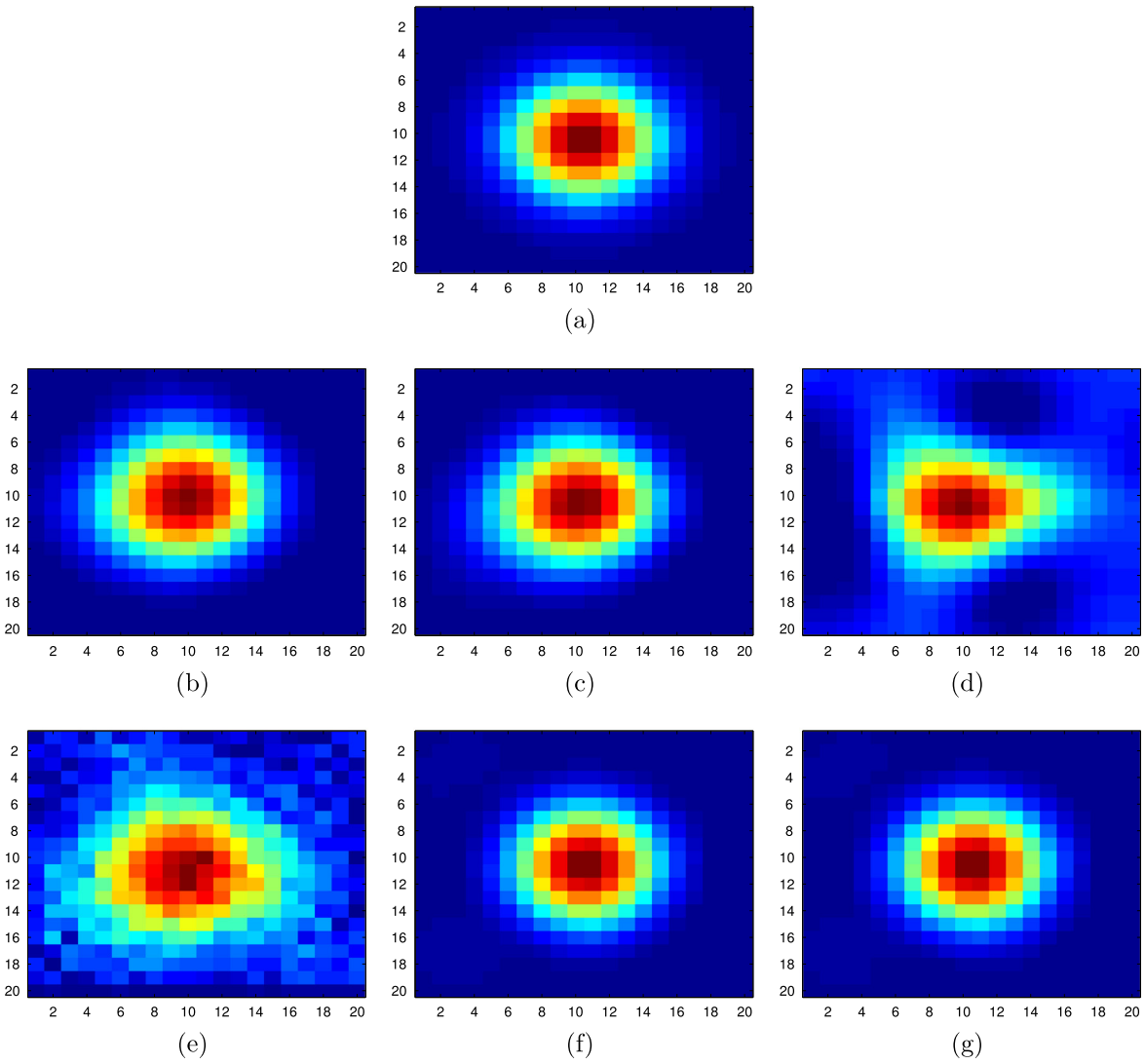

Fig. 6. The estimated kernels of different methods for the blurred microscopic image in Fig. 2(g). (a) The true kernel; (b) the estimated kernel of IWF, MSE $= 1.05 \times 10^{-6}$; (c) the estimated kernel of IWF-Phase&ESTV, MSE $= 7.85 \times 10^{-7}$; (d) the estimated kernel of method in [17], MSE $= 4.03 \times 10^{-6}$; (e) the estimated kernel of method in [20], MSE $= 5.33 \times 10^{-6}$; (f) the estimated kernel of the proposed IWF-H^1, MSE $= 1.90 \times 10^{-7}$; (g) the estimated kernel of the proposed IWF-TV, MSE $= 1.77 \times 10^{-7}$.

result of IWF-Phase&ESTV in Fig. 5(b), the ringing artifacts is slight but visible. The methods in [17] and [20] oversmooth the images, see Fig. 5(c)–(d). The results of the proposed algorithms in Fig. 5(e)–(f) seem satisfactory, which also have much higher PSNR values than others.

In Fig. 6, we display the estimated blur kernels for Im-7. Fig. 6(a) is the true Gaussian kernel with standard deviation 3 and size 20×20. Fig. 6(b)–(g) are the estimated kernels by six methods corresponding to the results in Fig. 5. Visually, the estimated kernels by the proposed methods are more close to the true kernel, see Fig. 6(f)–(g). For quantitative comparison, we calculate the mean square errors (MSE) of the estimated kernels and report them in the figure caption. Note that MSE is a standard measure for the estimating errors of kernels when the kernels are normalized and have the same size [45]. See [46] for other measures. It is obvious that the MSE of the proposed methods are much smaller than others, which implies that our methods give better estimation of the blur kernel.

4.2. Tests on real microscopic images

In this subsection, two real microscopic images as displayed in Fig. 7 are tested, which are also used in [8]. Fig. 7(a) was acquired on a confocal microscope with opened aperture. It has good signal intensity but gets blurred by the contributions

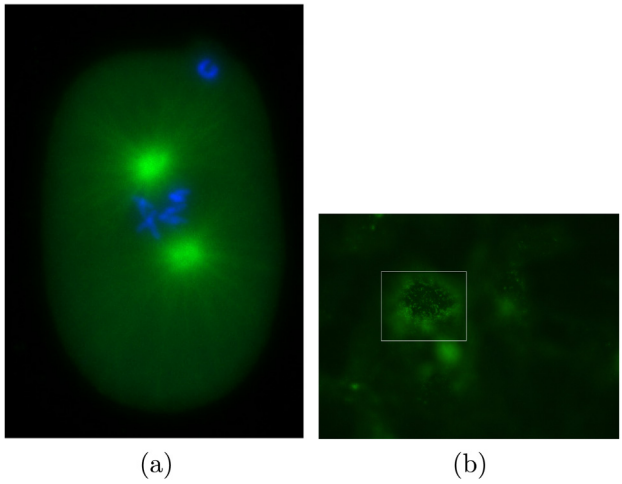

Fig. 7. Two real microscopic images for test.

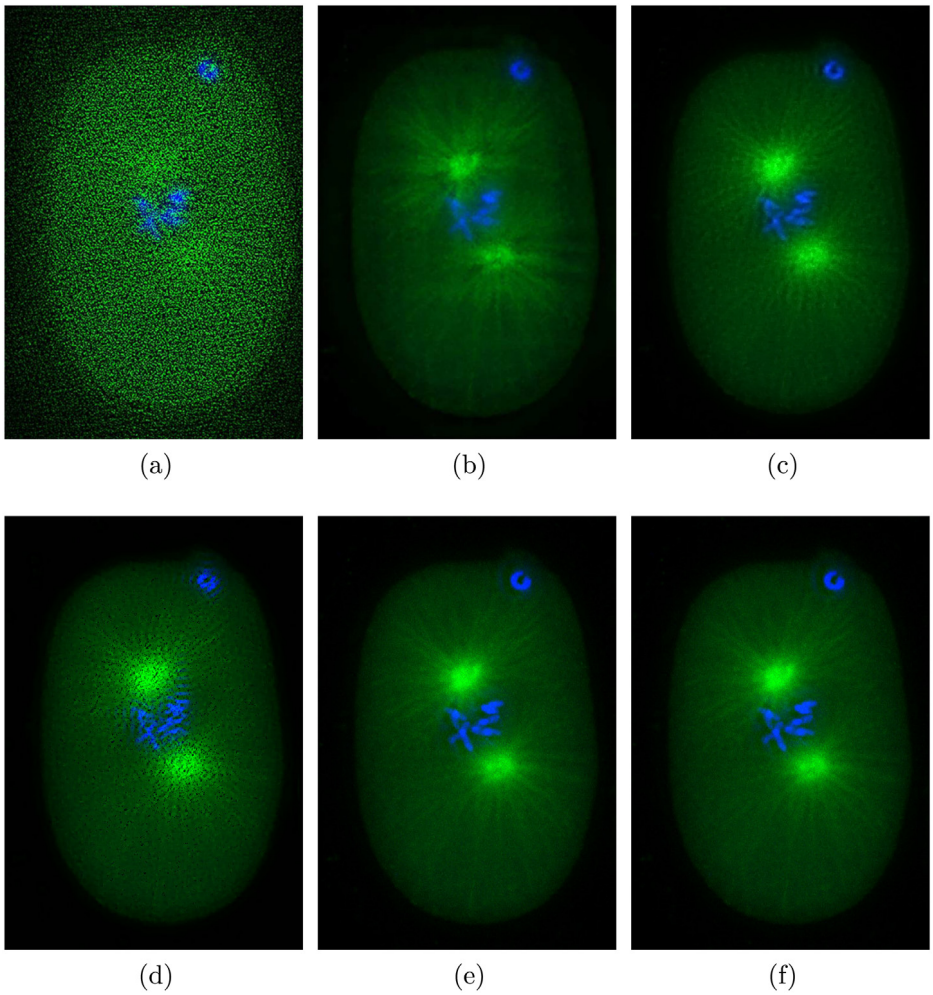

Fig. 8. Test on the real microscopic image in Fig. 7(a). (a) The result of IWF; (b) the result of IWF-Phase&ESTV; (c) the result of method in [17]; (d) the result of method in [20]; (e) the result of the proposed IWF-H^1; (f) the result of the proposed IWF-TV. (For interpretation of the references to color in this figure legend, the reader is referred to the web version of this article.)

Table 1
Deconvolution results for microscopic images degraded by Gaussian blur with standard deviation 3 and size 20 × 20. The PSNR (dB) values are reported for eight methods.

Image	Blurred	IWF	IWF-Phase	IWF-ESTV	IWF-Phase & ESTV	[17]	[20]	IWF-H^1	IWF-TV
im-1	35.58	35.36	35.35	35.54	36.07	33.78	28.82	**40.01**	39.87
im-2	34.93	35.51	35.24	35.82	36.69	35.10	31.64	38.31	**38.45**
im-3	34.43	36.12	36.51	36.74	37.58	32.57	31.92	**38.39**	38.34
im-4	34.14	36.40	36.37	36.59	37.89	33.26	30.62	37.88	**37.93**
im-5	36.42	41.16	41.18	41.43	41.76	35.00	31.30	**42.80**	42.74
im-6	35.23	38.74	39.51	39.34	40.31	34.25	31.74	40.72	**40.76**
im-7	38.55	40.37	41.16	40.63	42.59	35.60	33.62	**44.79**	44.70
im-8	35.94	37.89	38.70	38.33	39.82	36.26	33.64	**43.17**	43.04
im-9	34.84	37.20	36.23	37.38	36.66	36.06	30.52	**41.06**	41.05
im-10	33.90	38.03	36.95	38.27	38.50	34.46	32.95	**40.42**	40.39
im-11	35.34	38.54	37.39	38.81	38.78	35.71	36.47	**42.99**	42.95
im-12	34.48	36.24	36.20	36.57	37.28	35.09	33.83	**39.92**	38.06
im-13	37.12	40.00	39.36	40.29	40.55	35.50	32.79	42.30	**42.32**
im-14	37.59	40.02	40.37	40.65	42.28	34.19	35.12	44.68	**44.90**
Average	35.61	37.97	37.90	38.31	38.98	34.77	32.50	41.10	**41.11**

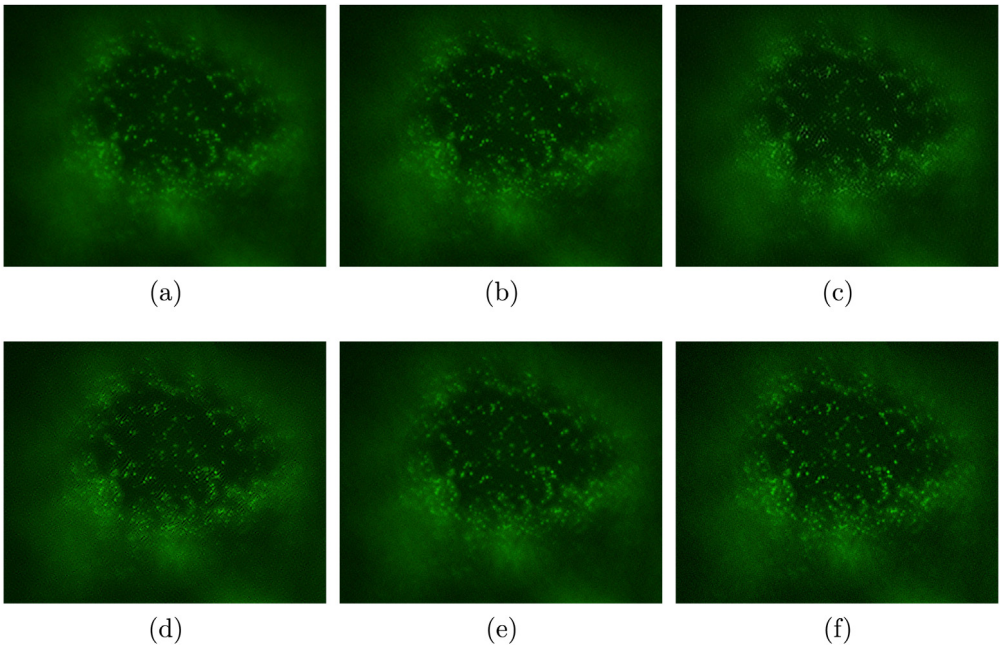

Fig. 9. Test on the real microscopic image in Fig. 7(b) (the subregion with rectangle is displayed). (a) The result of IWF; (b) the result of IWF-Phase&ESTV; (c) the result of method in [17]; (d) the result of method in [20]; (e) the result of the proposed IWF-H^1; (f) the result of the proposed IWF-TV.

of defocused objects, which are characteristic for widefield microscopes. Fig. 7(b) is a slice of immunofluorescence z-stacked images of CD133 positive Huh7 liver caner cells, see [8] for more details. As can be seen, the real microscopic images are very blurry.

In Fig. 8, we show the blind deconvolution results of Fig. 7(a) by applying six methods including IWF, IWF-Phase&ESTV, the methods in [17] and [20], the proposed IWF-H^1 and IWF-TV for visual comparison. Note that Fig. 8(a)–(b) are copied from [8]. Fig. 8(a) seems not converge. In Fig. 8(b), the blue objects seem still blurry. Fig. 8(c)–(d) have clear artifacts. The results of our proposed methods in Fig. 8(e)–(f) are satisfactory, both the green objects and the blue objects are well deblurred with sharp edges.

In Fig. 9, we show the blind deconvolution results of Fig. 7(b) by six different methods. For better visualization, we show a subregion which is marked by white rectangle in Fig. 7(b) for detail comparison. We can observe that Fig. 9(a)–(b) are still somewhat blurry and ring artifacts are obvious in Fig. 9(c)–(d). It seems that the proposed methods IWF-H^1 and IWF-TV give better deblurring results than others, see Fig. 9(e)–(f). For instance, the edges of the green spots are sharper than others and the ring artifacts are negligible.

5. Conclusion

The traditional IWF algorithm for blind image convolutions has two disadvantages: it is not stable and has serious ringing artifacts in many applications. To overcome the drawbacks, in this work, we have extended the IWF method by adding H^1 and TV regularization terms in an energy formulation and get two algorithms. Numerical results show that the proposed regularization algorithms are stable and can suppress ringing artifacts successfully. A limitation of the proposed methods, as well as the other IWF type methods, is that it is less effective for images with nonuniform black boundaries. In the future work, we will introduce other regularization techniques and combine our methods with other blind deconvolution methods to further enhance the image restoration quality and overcome its limitation. Theoretically, we will study the convergence behavior of the proposed algorithms.

References

[1] Anat Levin, Yair Weiss, Fredo Durand, William T. Freeman, Understanding blind deconvolution algorithms, IEEE Trans. Pattern Anal. Mach. Intell. 33 (12) (2011) 2354–2367.
[2] Deepa Kundur, Dimitrios Hatzinakos, Blind image deconvolution, IEEE Signal Process. Mag. 13 (3) (1996) 43–64.
[3] Norbert Wiener, Extrapolation, Interpolation, and Smoothing of Stationary Time Series, vol. 7, MIT Press, Cambridge, MA, 1949.
[4] C. Rafael Gonzalez, Richard Woods, Digital Image Processing, third ed., Pearson Education, 2007.
[5] William Hadley Richardson, Bayesian-based iterative method of image restoration, J. Opt. Soc. Amer. 62 (1) (1972) 55–59.
[6] Leon B. Lucy, An iterative technique for the rectification of observed distributions, Astron. J. 79 (1974) 745.
[7] G.R. Ayers, J. Christopher Dainty, Iterative blind deconvolution method and its applications, Opt. Lett. 13 (7) (1988) 547–549.
[8] Mohammad Tofighi, Onur Yorulmaz, Kivanç Köse, Deniz Cansen Yıldırım, Rengül Çetin-Atalay, A. Enis Çetin, Phase and tv based convex sets for blind deconvolution of microscopic images, IEEE J. Sel. Top. Sign. Proces. 10 (1) (2016) 81–91.
[9] D.A. Fish, J.G. Walker, A.M. Brinicombe, E.R. Pike, Blind deconvolution by means of the Richardson–Lucy algorithm, J. Opt. Soc. Am. A 12 (1) (1995) 58–65.
[10] David S.C. Biggs, Mark Andrews, Acceleration of iterative image restoration algorithms, Appl. Opt. 36 (8) (1997) 1766–1775.
[11] Nicolas Dey, Laure Blanc-Feraud, Christophe Zimmer, Pascal Roux, Zvi Kam, Jean-Christophe Olivo-Marin, Josiane Zerubia, Richardson–Lucy algorithm with total variation regularization for 3D confocal microscope deconvolution, Microsc. Res. Tech. 69 (4) (2006) 260–266.
[12] Martin Laasmaa, Marko Vendelin, Pearu Peterson, Application of regularized Richardson–Lucy algorithm for deconvolution of confocal microscopy images, J. Microsc. 243 (2) (2011) 124–140.
[13] J. Seo, S. Hwang, J.-M. LEE, H. Park, Spatially varying regularization of deconvolution in 3D microscopy, J. Microsc. 255 (2) (2014) 94–103.
[14] Yu-Li You, Mostafa Kaveh, A regularization approach to joint blur identification and image restoration, IEEE Trans. Image Process. 5 (3) (1996) 416–428.
[15] Tony F. Chan, Chiu-Kwong Wong, Total variation blind deconvolution, IEEE Trans. Image Process. 7 (3) (1998) 370–375.
[16] Leonid I. Rudin, Stanley Osher, Emad Fatemi, Nonlinear total variation based noise removal algorithms, Physica D 60 (1–4) (1992) 259–268.
[17] Dilip Krishnan, Terence Tay, Rob Fergus, Blind deconvolution using a normalized sparsity measure, in: Computer Vision and Pattern Recognition, CVPR, 2011 IEEE Conference on, IEEE, 2011, pp. 233–240.
[18] Rob Fergus, Barun Singh, Aaron Hertzmann, Sam T. Roweis, William T. Freeman, Removing camera shake from a single photograph, in: ACM Transactions on Graphics, TOG, vol. 25, ACM, 2006, pp. 787–794.
[19] Li Xu, Shicheng Zheng, Jiaya Jia, Unnatural l0 sparse representation for natural image deblurring, in: Proceedings of the IEEE Conference on Computer Vision and Pattern Recognition, 2013, pp. 1107–1114.
[20] Jinshan Pan, Zhe Hu, Zhixun Su, Ming-Hsuan Yang, L0-regularized intensity and gradient prior for deblurring text images and beyond, IEEE Trans. Pattern Anal. Mach. Intell. 39 (2) (2017) 342–355.
[21] Jian-Feng Cai, Hui Ji, Chaoqiang Liu, Zuowei Shen, Blind motion deblurring from a single image using sparse approximation, in: Computer Vision and Pattern Recognition, 2009. CVPR 2009. IEEE Conference on, IEEE, 2009, pp. 104–111.
[22] Jian-Feng Cai, Hui Ji, Chaoqiang Liu, Zuowei Shen, Framelet-based blind motion deblurring from a single image, IEEE Trans. Image Process. 21 (2) (2012) 562–572.
[23] Wenqi Ren, Xiaochun Cao, Jinshan Pan, Xiaojie Guo, Wangmeng Zuo, Ming-Hsuan Yang, Image deblurring via enhanced low-rank prior, IEEE Trans. Image Process. 25 (7) (2016) 3426–3437.
[24] Daniele Perrone, Paolo Favaro, Total variation blind deconvolution: the devil is in the details, in: Proceedings of the IEEE Conference on Computer Vision and Pattern Recognition, 2014, pp. 2909–2916.
[25] Weihong Li, Quanli Li, Weiguo Gong, Shu Tang, Total variation blind deconvolution employing split Bregman iteration, J. Vis. Commun. Image Represent. 23 (3) (2012) 409–417.
[26] Filip Sroubek, Peyman Milanfar, Robust multichannel blind deconvolution via fast alternating minimization, IEEE Trans. Image Process. 21 (4) (2012) 1687–1700.
[27] Jun Zhang, Kwok-Wing Chau, et al., Multilayer ensemble pruning via novel multi-sub-swarm particle swarm optimization, J. UCS 15 (4) (2009) 840–858.
[28] Shanwen Zhang, Kwok-Wing Chau, Dimension reduction using semi-supervised locally linear embedding for plant leaf classification, Emerg. Intell. Comput. Technol. Appl. (2009) 948–955.
[29] K.W. Chau, C.L. Wu, A hybrid model coupled with singular spectrum analysis for daily rainfall prediction, J. Hydroinform. 12 (4) (2010) 458–473.
[30] Riccardo Taormina, Kwok-Wing Chau, Data-driven input variable selection for rainfall–runoff modeling using binary-coded particle swarm optimization and Extreme Learning Machines, J. Hydrol. 529 (2015) 1617–1632.
[31] Chenglong Bao, Bin Dong, Likun Hou, Zuowei Shen, Xiaoqun Zhang, Xue Zhang, Image restoration by minimizing zero norm of wavelet frame coefficients, Inverse Problems 32 (11) (2016) 115004.
[32] Chunlin Wu, Xue-Cheng Tai, Augmented Lagrangian method, dual methods, and split Bregman iteration for ROF, vectorial TV, and high order models, SIAM J. Imaging Sci. 3 (3) (2010) 300–339.
[33] Benxin Zhang, Zhibin Zhu, et al., A modified spectral conjugate gradient projection algorithm for total variation image restoration, Appl. Math. Lett. 27 (2014) 26–35.
[34] Ernie Esser, Xiaoqun Zhang, Tony F. Chan, A general framework for a class of first order primal-dual algorithms for convex optimization in imaging science, SIAM J. Imaging Sci. 3 (4) (2010) 1015–1046.
[35] Antonin Chambolle, Thomas Pock, A first-order primal-dual algorithm for convex problems with applications to imaging, J. Math. Imaging Vis. 40 (1) (2011) 120–145.

[36] Tom Goldstein, Stanley Osher, The split Bregman method for L1-regularized problems, SIAM J. Imaging Sci. 2 (2) (2009) 323–343.
[37] Fang Li, Tieyong Zeng, A universal variational framework for sparsity-based image inpainting, IEEE Trans. Image Process. 23 (10) (2014) 4242–4254.
[38] Jian-Feng Cai, Bin Dong, Stanley Osher, Zuowei Shen, Image restoration: total variation, wavelet frames, and beyond, J. Amer. Math. Soc. 25 (4) (2012) 1033–1089.
[39] Guy Gilboa, Stanley Osher, Nonlocal operators with applications to image processing, Multiscale Model. Simul. 7 (3) (2008) 1005–1028.
[40] Marius Lysaker, Arvid Lundervold, Xue-Cheng Tai, Noise removal using fourth-order partial differential equation with applications to medical magnetic resonance images in space and time, IEEE Trans. Image Process. 12 (12) (2003) 1579–1590.
[41] Fang Li, Chaomin Shen, Jingsong Fan, Chunli Shen, Image restoration combining a total variational filter and a fourth-order filter, J. Vis. Commun. Image Represent. 18 (4) (2007) 322–330.
[42] Praveen Pankajakshan, Bo Zhang, Laure Blanc-Féraud, Zvi Kam, Jean-Christophe Olivo-Marin, Josiane Zerubia, Blind deconvolution for thin-layered confocal imaging, Appl. Opt. 48 (22) (2009) 4437–4448.
[43] Bo Zhang, Josiane Zerubia, Jean-Christophe Olivo-Marin, Gaussian approximations of fluorescence microscope point-spread function models, Appl. Opt. 46 (10) (2007) 1819–1829.
[44] Ece Akhan, Donus Tuncel, Kamil C. Akcali, Nanoparticle labeling of bone marrow-derived rat mesenchymal stem cells: their use in differentiation and tracking, Biomed. Res. Internat. 2015 (2015).
[45] Christian J. Schuler, Michael Hirsch, Stefan Harmeling, Bernhard Schölkopf, Learning to deblur, IEEE Trans. Pattern Anal. Mach. Intell. 38 (7) (2016) 1439–1451.
[46] Anat Levin, Yair Weiss, Fredo Durand, William T. Freeman, Understanding and evaluating blind deconvolution algorithms, in: Computer Vision and Pattern Recognition, 2009. CVPR 2009. IEEE Conference on, IEEE, 2009, pp. 1964–1971.